Simulations of Deep Exclusive $\pi^0, \eta, \rho, \omega, \eta', \phi$ Meson Production at Jefferson Lab Hall C

Physics 499 Thesis

Michael Hladun

Department of Physics

University of Regina

Regina, SK, Canada

April 23, 2018

Abstract

For the first time, the $p(e, e'K^+)\Lambda, \Sigma^0$ reaction will be studied above the resonance region with the intent of extracting the separated cross sections (L/T/LT/TT) using the Rosenbluth separation technique. During the experiment, $p(e, e'p)\pi^0, \eta, \rho, \omega, \eta', \phi$ reactions will also be detected. The kinematic settings used in this experiment range from 0.40 GeV^2 $\leq Q^2 \leq$ 5.5 GeV^2 (photon virtuality) with 2.32 GeV $\leq W \leq$ 3.37 GeV (hadronic invariant mass) and 0.064 GeV^2 $\leq -t \leq$ 0.531 GeV^2 (four momentum transfer). By using these settings in the SIMC (Standard Hall C Monte Carlo package) simulations, estimates of backward-angle meson production rates were determined, and the feasibility of their measurements was studied.

Acknowledgements

I would like to thank Dr. Garth Huber for sharing his expertise in subatomic physics with me during this project. His organization skills and work ethic made this project achievable.

A special thanks to Samip Basnet who guided me through this project while simultaneously working on his Doctorate in Physics. His commitment towards helping me accomplish this project was very generous.

Contents

List of Figures

List of Tables

List of Abbreviations

- SIMC - Single Arm Monte Carlo package/Standard Hall C Monte Carlo package
- DIS - deep inelastic scattering
- pQCD - perturbative quantum chromodynamics
- PMT - photo-multiplier tube
- TOF - time of flight
- ${}^1H(e,e'p)\pi^0,\eta,\rho,\omega,\eta',\phi$ is a notation used to describe a set of particles in a given reaction. A template for this notation: target(beam, detected particles)reconstructed particles.

Chapter 1

Introduction

The Standard Model consists of an array of elementary particles (see Figure 1). Hadrons are combinations of elementary particles called quarks. They consist of baryons, which contain three valence quarks (qqq), and mesons, which contain one quark and one antiquark ($q\overline{q}$). All quarks interact via weak, electromagnetic and strong forces.

The field theory used to describe the electromagnetic interaction is quantum electrodynamics (QED). The force carrier for the electromagnetic interaction is the photon. The intensity of the electromagnetic interaction is characterized by the electromagnetic coupling constant, $\alpha_e \approx \frac{1}{137}$.

The field theory used to describe the strong interaction is quantum chromodynamics (QCD), and its force carrier is the gluon, which transmits colour charge between quarks. Unlike photons, gluons can interact with one another, and the intensity of the strong interaction is characterized by the strong coupling constant, α_s, which changes with distance scales. At high energies, which correspond to short distance interaction scales ($\sim 10^{-17}$m), α_s becomes small. The opposite it true for α_s at low energies; it corresponds to long dis-

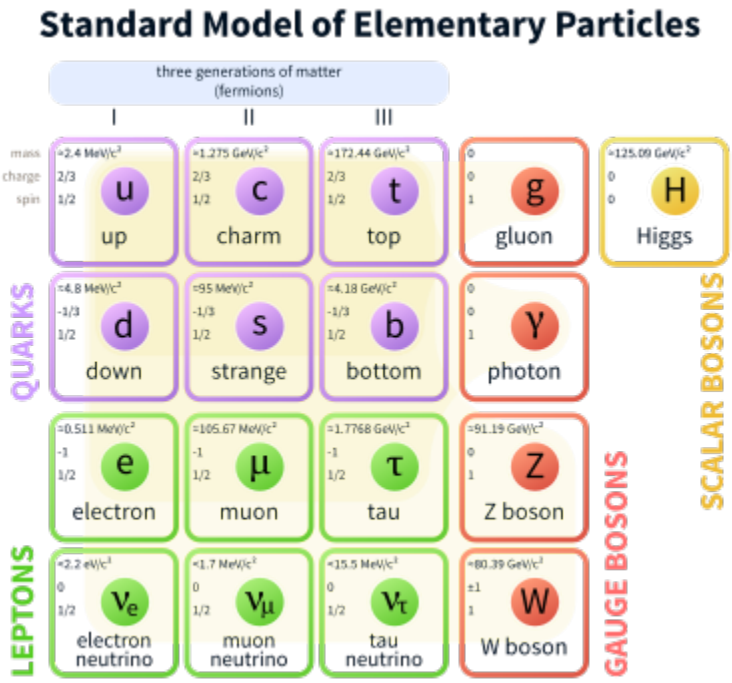

Figure 1: The Standard Model of Particle Physics

tance interaction scales ($\sim 10^{-15}$m) with α_s becoming larger (see Figure 2). At high energies, perturbative QCD (pQCD) accurately represents quark-gluon interactions since the forces between quarks and gluons (partons) are abysmal.

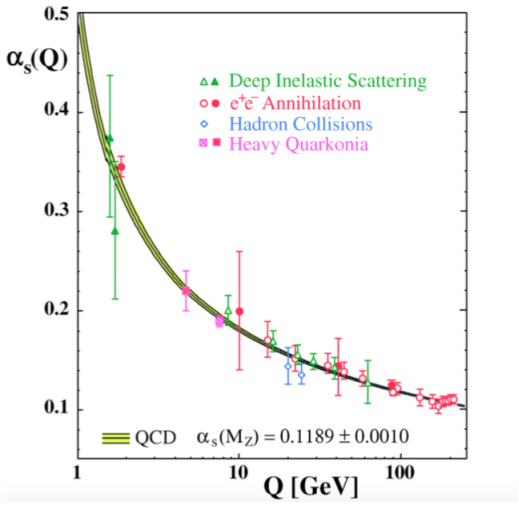

Figure 2: A plot of α_s as a function of Q. The curves are the QCD predictions for the combined world average value of $\alpha_s(M_{Z^0})$. [3].

This undergraduate work is part of the effort to understand hadronic structures at intermediate energies of $\sim$ 1-10 GeV. This work determines the estimates of backward-angle meson production rates, and the feasibility of backward-angle meson measurements for Jefferson Lab's experiment, E12-09-011. Experiment E12-09-011's main focus is the study of the $p(e, e'K^+)\Lambda, \Sigma^0$ reaction above the resonance region for the first time. However, it is anticipated that complementary information on backward-angle meson electroproduction can be extracted from this experiment. The backward-angle mesons studied in this work are $\pi^0, \eta, \rho, \omega, \eta', \phi$. A list of their characteristics can be found in Table 1.1.

	Meson	**Valence Quarks**	**Rest Mass (MeV/c^2)**	**Full Width (MeV)**
Vectors: $(J^P = 1^-)$	ρ^0	$\frac{u\bar{u}-d\bar{d}}{\sqrt{2}}$	775.26 $\pm$ 0.25	149.1 $\pm$ 0.8
	ω	$\frac{u\bar{u}-d\bar{d}}{\sqrt{2}}$	782.65 $\pm$ 0.12	8.49 $\pm$ 0.08
	ϕ	$s\bar{s}$	1019.46 $\pm$ 0.019	4.266 $\pm$ 0.031
Pseudoscalars: $(J^P = 0^-)$	π^0	$\frac{u\bar{u}-d\bar{d}}{\sqrt{2}}$	134.9766 $\pm$ 0.0006	4.536 $\pm$ 0.0005
	η	$\frac{u\bar{u}+d\bar{d}-2s\bar{s}}{\sqrt{3}}$	547.862 $\pm$ 0.0018	0.00131 $\pm$ 0.00005
	η'	$\frac{u\bar{u}+d\bar{d}+s\bar{s}}{\sqrt{6}}$	957.78 $\pm$ 0.06	0.198 $\pm$ 0.009

Table 1.1: The mesons studied in this work along with some of their general properties. These values are taken from [5].

1.1 Deep Exclusive Inelastic Scattering Overview

To study hadrons, scientists use a variety of scattering techniques. In this work, *deep exclusive inelastic scattering* is used to study the proton at energies on the order of 1-10 GeV. *Deep* pertains to a hard scattering from the constituents within a nucleon, allowing

the partonic degrees of freedom within a nucleon to be studied, opposed to hadronic degrees of freedom. *Exclusive* refers to each of the particles in the reaction having their energy and momenta observed or uniquely reconstructed. If this is not the case, the reaction is said to be *inclusive*. Lastly, *inelastic* means the incoming particle's kinetic energy is not conserved. Figure 3 (b) demonstrates an electron's kinetic energy being transferred to a proton, via a photon, allowing the formation of hadrons.

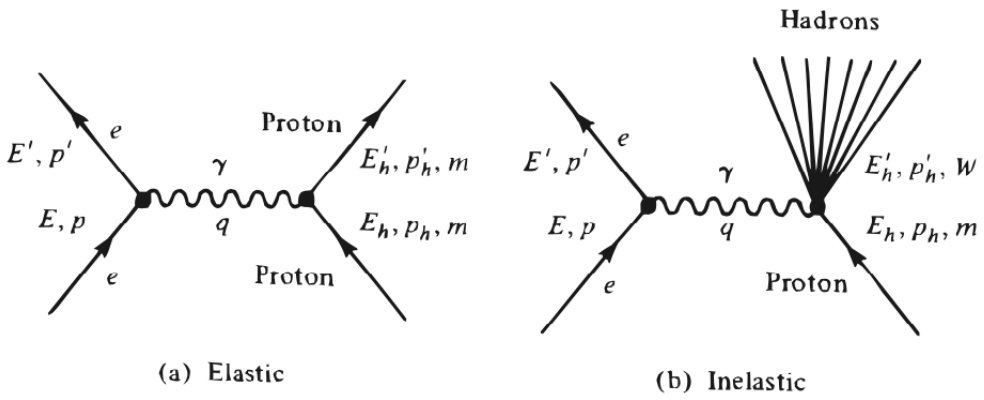

Figure 3: Feynman diagrams for elastic and inelastic electron-proton scattering. Time flows upwards. [1]

Electrons make good deep inelastic scattering (DIS) probes because of their point-like nature, and because the field theory of their electromagnetic interactions, QED, is a well developed/successful theory. The electromagnetic interaction between an electron and a hadron target can be described by the exchange of a single virtual photon. Virtual photons arise due to Heisenberg's Uncertainty Principle, and have the properties of being time-like ($E^2 - p^2 > 0$), or space-like ($E^2 - p^2 < 0$). The virtual photons in this work are space-like.

The energy and momentum with which a virtual photon, γ^*, interacts with a hadron target greatly effects the probed distance scale. At low energy and momentum transfer, γ^* can interact with with an entire nucleus as it scatters elastically, or inelastically, with the

possibility of creating nuclear resonances. At higher energy and momentum transfer, in the quasi-elastic scattering region, individual nucleons can be probed, and excited into resonance states such as the Δ baryons (Δ^{++} with constituent quarks uuu, Δ^{+} with constituent quarks uud, etc.). Still, at even higher energies and momenta, γ^* becomes more sensitive to shorter distance scales, and reveals partonic degrees of freedom. The shifting of probed distance scales is depicted in Figure 4 as a function of scattered electron energy.

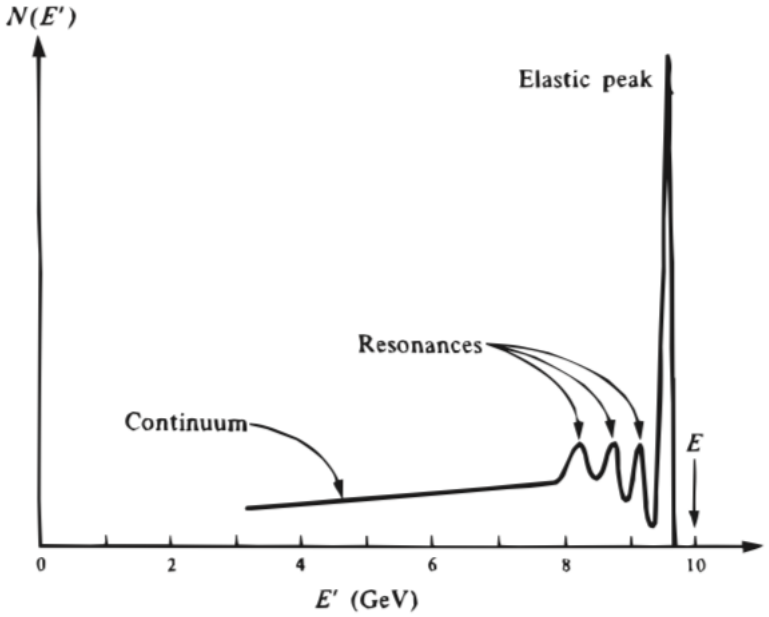

Figure 4: An illustration of the shifting from high electron momentum transfer to low electron momentum transfer. This also illustrates the shift from partonic to hadronic degrees of freedom. N(E′) gives the number of scattered electrons with energy E′. The "elastic peak" corresponds to probing a nucleus structure. The "resonances" corresponds to probing nucleus and nucleon structures. The "continuum", the energy region this work is considering, corresponds to probing the nucleon's parton distribution. [1]

1.2 Experimental Overview

In fall 2018, the K^+ experiment at Jefferson Lab, also known as experiment E12-09-011 [2], will consist of a 70 μA electron beam directed at a liquid hydrogen container acting

as a proton target. The focus of this interaction is to produce K^+'s, Λ's, and Σ^0's in the following reactions:

$$\begin{aligned} e + p &\rightarrow e' + K^+ + \Lambda \\ e + p &\rightarrow e' + K^+ + \Sigma^0 \end{aligned} \tag{1.1}$$

This experiment will be studying the exculsive electroproduction of K^+ above the resonance region for the first time ever. These interactions can be represented more efficiently by using the notation $p(e, e'K^+)\Lambda, \Sigma^0$ where p is the target, e is the beam, e' and K^+ are measured by the HMS and SHMS respectively, and Λ and Σ^0 are reconstructed particles. The kinematic settings for this experiment are outlined in Table 1.2.

It is anticipated that backward-angle mesons can be studied using the same settings as in the K^+ experiment. In this case, we will have the reactions $p(e, e'p)\pi^0, \eta, \rho, \omega, \eta', \phi$. The electrons will be detected using the High Momentum Spectrometer (HMS) and the protons will be detected using the Super High Momentum Spectrometer (SHMS). The $\pi^0, \eta, \rho, \omega, \eta', \phi$, mesons produced in DIS will have their energy and momentum reconstructed. Note that for the rest of this work, X will define the set of mesons $\{\pi^0, \eta, \rho, \omega, \eta', \phi\}$. The mass of the undetected mesons can be inferred via the missing mass technique, where an expression for the missing mass can be derived by using,

$$\begin{aligned} E_m &= E_e - E_{e'} - E_p \\ \vec{p}_m &= \vec{p}_e - \vec{p}_{e'} - \vec{p}_p = \vec{q} - \vec{p}_p \end{aligned} \tag{1.2}$$

giving $M_m = \sqrt{{E_m}^2 - \overrightarrow{p_m}^2}$.

Q^2 (GeV^2)	W (GeV)	x_B	$-t$ (GeV^2)	ϵ	T_{inc} (GeV)	$T_{e'}$ (GeV)	$\theta_{e'}$ (deg)	θ_q (deg)	P_p (GeV/c)	θ_{pq} (deg)
Study of the reaction mechanism and form factor Q^2 dependence:										
0.40	2.45	0.072	0.064	0.411	3.799	0.857	20.2	-5.6	2.669	0,+3
0.40	2.45	0.072	0.064	0.685	4.951	2.008	11.5	-7.7	2.669	-2.15,0,+3
1.25	3.14	0.122	0.084	0.492	7.495	2.044	16.4	-6.0	5.189	0,+3
1.25	3.14	0.122	0.084	0.699	9.343	3.892	10.6	-7.4	5.189	-1.9,0,+3
2.00	3.14	0.182	0.138	0.395	7.495	1.645	23.2	-6.2	5.561	0,+3
2.00	3.14	0.182	0.138	0.580	8.761	2.910	16.1	-7.7	5.561	-2.2,0,+3
2.00	3.14	0.182	0.138	0.752	10.921	5.070	10.9	-9.2	5.561	-3,0,+3
3.00	3.14	0.250	0.219	0.391	8.191	1.807	26.0	-6.9	6.053	0,+3
3.00	3.14	0.250	0.219	0.691	10.921	4.537	14.1	-9.6	6.053	-3,0,+3
Scaling study at fixed x_B = 0.25, -t=0.2:										
1.70	2.45	0.249	0.239	0.595	5.647	2.012	22.3	-11.4	3.277	0,+3
1.70	2.45	0.249	0.239	0.856	8.761	5.125	11.6	-14.9	3.277	-3,0,+3
3.50	3.37	0.250	0.215	0.364	9.343	1.895	25.7	-6.1	7.122	0,+3
3.50	3.37	0.250	0.215	0.557	10.921	3.473	17.5	-7.8	7.122	-3,0,+3
Scaling study at fixed x_B = 0.40, -t = 0.5:										
3.00	2.32	0.400	0.531	0.634	6.601	2.603	24.1	-14.1	3.486	0,+3
3.00	2.32	0.400	0.531	0.888	10.921	6.923	11.4	-18.4	3.486	-3,0,+3
4.40	2.74	0.399	0.507	0.479	8.191	2.314	27.9	-10.0	5.389	0,+3
4.40	2.74	0.399	0.507	0.735	10.921	5.045	16.3	-13.1	5.389	-3,0,+3
5.50	3.02	0.400	0.503	0.372	9.343	2.021	31.3	-7.9	6.842	0,+3
5.50	3.02	0.400	0.503	0.562	10.921	3.599	21.6	-9.9	6.842	-3,0,+3

Table 1.2: Kinematic settings for exclusive K^+ electroproduction above the resonance region. These are the same settings which have been used in this work's simulations to study $\pi^0, \eta, \rho, \omega, \eta', \phi$ reactions. Q^2 is the four momentum (defined as $Q^2 = |\vec{p_e} - \vec{p_{e'}}|^2 - (E_i - E_f)^2$), W is the invariant mass (defined as $\sqrt{s}$; see Equation 1.3), x_B is the Bjorken scaling factor (defined in Equation 1.5), $-t$ is a Mandelstam variable (defined in Equation 1.3), ϵ is the virtual photon polarization factor (defined in Equation 1.6), T_{inc} and $T_{e'}$ are the initial and scattered electron beam energies, respectively, $\theta_{e'}$ is the angle between the incoming and scattered electron, "θ_q gives the direction of the virtual photon which corresponds to the nominal angle of [SHMS]" [4], P_p is the proton recoil momentum, and lastly, θ_{pq} is the angle between the recoiled proton and q (positive angles represent rotations away from the beam line) [4]. Table from [7].

Here $\vec{q}$ is the 3-momentum vector of the virtual photon ($\vec{q} = \vec{p}_e - \vec{p}_{e'}$). The transferred four-momentum of the virtual photon is given by $q^2 = q_\mu q^\mu = \omega^2 - |\vec{q}|^2$, where $\omega = (E_i - E_f)$ and $\hbar = 1$. In this work, $q^2 < 0$ because the electron scattering process is space-like. The

variable Q^2 is a Lorentz invariant quantity defined by $Q^2 = -q^2$. Besides Q^2, other Lorentz invariant quantities can be defined including,

$$\begin{aligned} s &= (p_H + q)^2 = (p_p + p_X)^2 \\ t &= (p_H - p_p)^2 = (q - p_X)^2 \\ u &= (p_H - p_X)^2 = (q - p_p)^2 \end{aligned} \tag{1.3}$$

These variables are called Mandelstam variables, and they can be used to define a series of scattering interaction channel types as shown in Figure 5. In this definition of Mandelstam variables, H denotes the proton before the interaction, q is the virtual photon's 3-momentum, p denotes the recoiled proton, and X denotes the set of backward angle mesons. The square-root of s is the invariant mass of the hadronic system, t is the four momentum transfer squared between the proton before and after the interaction, and u is the four momentum transfer squared between the virtual photon before the interaction and the proton after interaction. s describes the energy region where the interaction is taking place, t describes how forward a produced meson can go, and u describes how backward a produced meson can go. These variables obey the principle,

$$s + t + u = m_H^2 + m_{\gamma^*}^2 + m_p^2 + m_M^2 \tag{1.4}$$

which is useful for making physical assertions in Monte Carlo simulations.

Figures 6 and 7 contrast the difference between backward and forward angle produced mesons. Forward angle production is also referred to as a t-channel process, while backward angle production is also referred to as a u-channel process.

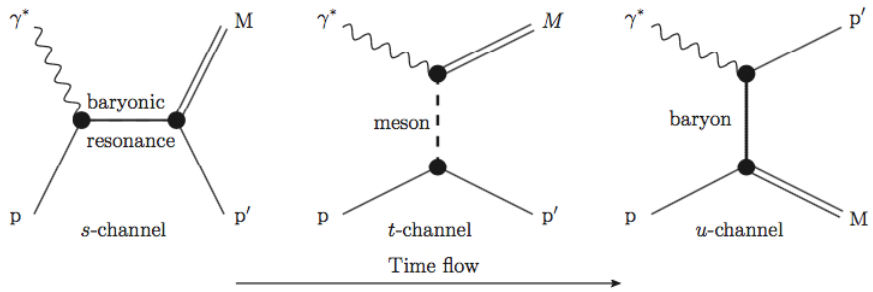

Figure 5: Schematic diagrams for s, t and u channel scattering interactions. [4]

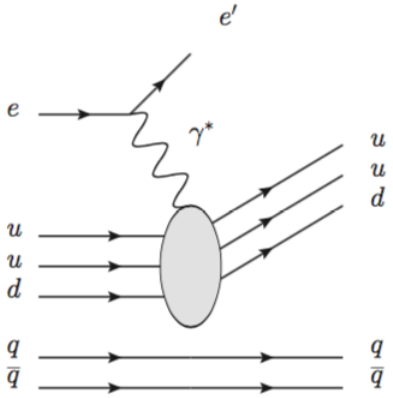

Figure 6: A schematic for backward angle meson production. $uudq\bar{q}$ on the left hand side of the schematic represents a proton, uud, with non-valence quarks, $q\bar{q}$. The virtual photon emitted by the scattered electron *knocks the proton out of the proton.* $q\bar{q}$ is a meson, X, produced from this process. Time goes from left to right.

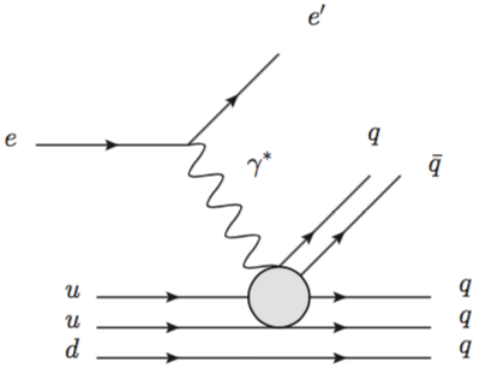

Figure 7: A schematic for forward angle meson production. uud on the left hand side of the schematic represents a proton interacting with a virtual photon, emitted via an electron, knocking a meson, $q\bar{q}$, out of the proton, giving rise to a baryon, qqq. Time goes from left to right.

The cross sections of mesons, X, will be calculated using the Rosenbluth Separation technique which requires two or more reaction measurements at the same W (hadron invariant mass), Q^2 (virtual photon momentum transfer), $-t$ (four momentum transfer of the proton before and after the interaction), and x_B (Bjorken scaling factor), but different ϵ (virtual photon longitudinal polarization) to making extracting cross sections possible. The Bjorken scaling factor, x_B, is expressed as

$$x_B = \frac{Q^2}{2m_p\nu}, \tag{1.5}$$

where m_p is the proton mass, and $\nu \equiv (E_e - E_e{}')$. It represents the fraction of momentum carried by a struck particle. In the case of a virtual photon hitting a valence quark (as opposed to a non-valence quark), x_B should be close to 0.3 because protons have three valence quarks (uud). The virtual photon longitudinal polarization, ϵ, is expressed as

$$\epsilon = \Big[1 + \frac{2|\vec{q}|^2}{Q^2}\tan^2\Big(\frac{\theta_e}{2}\Big)\Big]^{-1}. \tag{1.6}$$

It represents the fraction of longitudinally polarized virtual photons over transversely polarized virtual photons ($\epsilon = \gamma_L^*/\gamma_T^*$). The equation used to calculate the cross sections comes from the contraction of a lepton tensor $L_{\mu\nu}$ and a hadron tensor $W^{\mu\nu}$,

$$\frac{d^5\sigma}{d\Omega_{e'}dE_{e'}d\Omega_p} = \frac{|p_p|E_p\alpha^2E_{e'}}{Q^4E_e}L_{\mu\nu}W^{\mu\nu} \tag{1.7}$$

With some work, the five-fold differential cross section in Equation 1.7 can be reduced to

the following equation,

$$2\pi\frac{d^2\sigma}{dtd\phi} = \frac{d\sigma_T}{dt} + \epsilon\frac{d\sigma_L}{dt} + \sqrt{2\epsilon(1+\epsilon)}\frac{d\sigma_{LT}}{dt}\cos(\phi) + \epsilon\frac{d\sigma_{TT}}{dt}\cos(2\phi) \tag{1.8}$$

To perform L-T-LT-TT cross section separations, measurements are taken over full ϕ coverage, removing the factor of 2π as well as all ϕ dependence. Integration over the experimental acceptance is then performed, making Equation 1.8 free of interference terms, $d\sigma_{LT}$ and $d\sigma_{TT}$. After these manipulations, Equation 1.8 takes on the form

$$\frac{d\sigma}{dt} = \frac{d\sigma_T}{dt} + \epsilon\frac{d\sigma_L}{dt}. \tag{1.9}$$

To separate σ_L and σ_T, measurements are taken at high and low ϵ. This gives us the following equations for σ_L and σ_T:

$$\frac{d\sigma_L}{dt} = \frac{\left(\frac{d\sigma}{dt}\right)_{\text{High}} - \left(\frac{d\sigma}{dt}\right)_{\text{Low}}}{\epsilon_{\text{High}} - \epsilon_{\text{Low}}} \tag{1.10}$$

$$\frac{d\sigma_T}{dt} = \frac{\epsilon_{\text{High}}\left(\frac{d\sigma}{dt}\right)_{\text{Low}} - \epsilon_{\text{Low}}\left(\frac{d\sigma}{dt}\right)_{\text{High}}}{\epsilon_{\text{High}} - \epsilon_{\text{Low}}} \tag{1.11}$$

Equations 1.10 and 1.11 show how choosing kinematic settings in pairs is necessary in order to extract transverse and longitudinal cross section since they rely on two different ϵ settings, ϵ_{High} and ϵ_{Low}, while measuring the same cross section, $d\sigma/dt$ (with the exception of ϵ dependence). This constrains the use of data to the overlapping regions of W and Q^2 for calculating cross sections. Other data is discarded. This will be more evident in Section 2.2

with the introduction of diamond plots.

1.2.1 Kinematics

In the interactions, the scattering plane is defined by the electron and scattered electron three vectors, $\vec{p_e}$ and $\vec{p_e}'$. The reaction plane is defined by the proton and meson three vectors, $\vec{p_p}$ and $\vec{p_X}$. In the interaction plane, the scattered electron, e', makes an angle θ_e with respect to e in the lab frame. The azimuthal angle between the scattering plane, and the reaction plane is ϕ_X ($\phi_p = \phi_X + 180^o$). These quantities are illustrated in Figure 8 where a meson from set X is chosen to be ω.

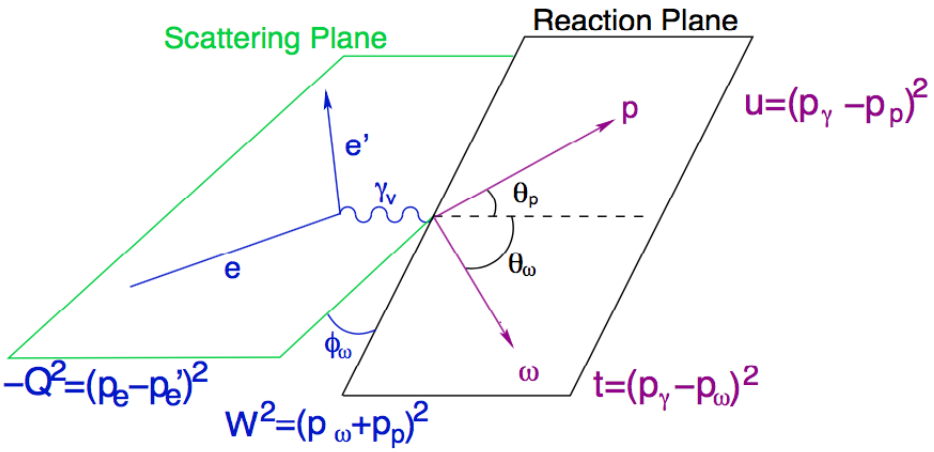

Figure 8: The scattering and reaction planes for the ω production interaction: $p(e, e'p)\omega$. The scattering plane is shown in green box and the reaction plane is shown in black box. γ_ν represents the exchanged virtual photon, p represents the recoiled proton, θ_p and θ_ω are angles with respect to the q-vector. [4]

1.2.2 LH_2 Target

For this experiment, a liquid hydrogen target, LH_2, is used as a proton target. Its container is a 4.0 cm in diameter cylinder orientated vertically. The container walls are

made from 0.0127cm thick aluminum alloy A1-T6061 [9]. The target is cooled by 15 K liquid helium, which keeps the LH_2 target at a temperature of 19 K and a pressure of 166kPa, resulting in a density of 0.0723 ± 0.0005 g/cm^3.

1.2.3 Spectrometers

The HMS and SHMS are both small solid angle magnetic focusing spectrometers at Jefferson Lab Hall C. This means the electrons and protons, which are detected by the HMS and SHMS respectively, can have their solid angles measured with high precision. In both spectrometers, three quadrupole magnets focus the outgoing particles into a vertical-bending dipole magnet which disperses particles based on their charge and momentum. The particle's momentum is determined from their position and crossing angle at the focal plane where a series of tracking and particle identification detectors are located in a shielded hut. A schematic of the two spectrometers can be viewed in Figure 9.

HMS and SHMS performance and design parameters are outlined in Table 1.3. Before the introduction of the SHMS, there was the short orbit spectrometer (SOS) and the HMS. The SOS had lesser performance capabilities than the HMS, and now its replacement, SHMS, has greater performance capabilities, which comes mainly from the higher central momentum range.

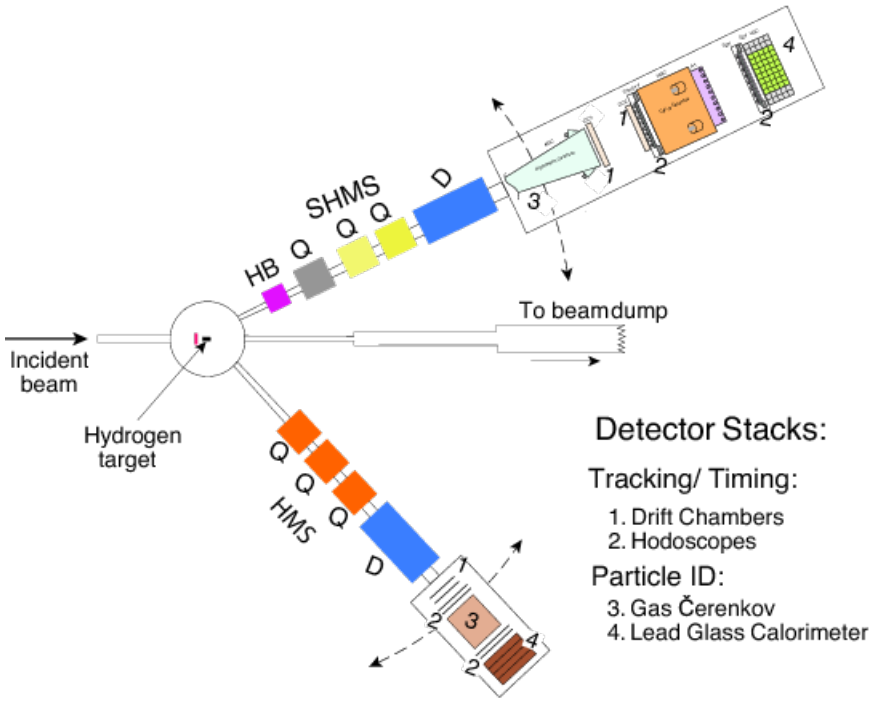

Figure 9: A schematic of the spectrometers at Jefferson Lab Hall C. HB represents a horizontal bending magnet, Q represents quadrupole magnets, D represents vertical-bending dipole magnets. [6]

Quantity	**Specifications**	
	HMS	**SHMS**
Dipole Bend Angle (^{o})	25.0	18.4
Central Momentum Range (GeV/c)	0.5-7.5	2.0-11.0
Path Length (m)	26.0	18.1
Scattering Angle Range (^{o})	12.5-90	5.5-40.0
Momentum Acceptance ($\delta p/p$)	$\pm$10.0%	-10% $< \delta <$ +22%
Momentum Resolution	$< 0.1\%$	$0.03 - 0.08\%$
Solid Angle Acceptance (msr)	6.7	4.0
Horizontal Acceptance (mrad)	$\pm$27.5	$\pm$24.0
Vertical Resolution (mrad)	$\pm$70.0	$\pm$40.0
Horizontal Resolution (mrad)	0.8	0.5-1.2
Vertical Resolution (mrad)	0.9	0.3-1.1
Maximum DAQ Rate (events/second)	$\sim$10000	$\sim$10000

Table 1.3: The performance and design parameters comparison between HMS and SHMS. [8]

Both of the spectrometers use similar detector packages consisting of: drift chambers, for

measuring particle coordinates and trajectories, hodoscopes, for calculating time-of-flight (TOF) and implementing trigger systems, heavy gas Čerenkov detectors, for $e-\pi$ separation, aerogel Čerenkov detectors, for proton$-\pi$ separation, and lead glass calorimeters, for particle identification.

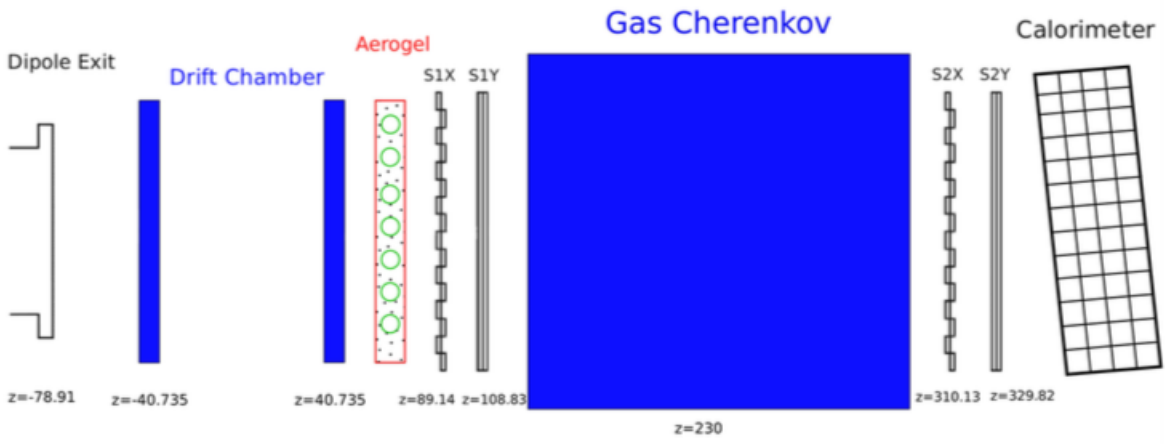

Figure 10: A schematic of the spectrometers at Hall C. [4]

The spectrometer's drift chambers are used to calculate charged particle trajectories and momenta by measuring their positions before and after the focal plane. They are filled with argon and ethane (inert gas) at a 1:1 ratio, and are threaded with six planes of sense wires, x, y, u, v, y', x', each separated by 1 cm. x measures the vertical coordinates of particle trajectories, and y measures the horizontal coordinates. The u and v planes are aligned $\pm 15^{o}$ with respect to the x plane in order to increase tracking resolution in the vertical direction. When charged particles enter the drift chambers, they ionize the inert gas, and the ionized electrons are captured by the sense wires, providing a way of acquiring the location of the charged particle.

The hodoscopes consist of horizontal and vertical planes of scintillators attached to photo-multiplier tubes (PMT's) placed before and after the Čerenkov detectors. The hodoscopes

purpose is to measure the time-of-flight of charged particles, and allow the implementation of a trigger system. When charged particles pass through the scintillators, atomic electrons are ionized and emitted within the scintillator. These emitted electrons excite other molecules in the scintillator which subsequently de-excite into their ground states by emitting photons. These de-excitation photons are detected by the PMT's attached to the ends of the scintillators.

The heavy gas Čerenkov (HGC) detectors are used to separate pions and electrons. Charged particles emit photons collectively known as Čerenkov radiation when they travel faster than the phase velocity of light in a dielectric medium. In this experiment, the Čerenkov medium is perflubutane (C_4F_{10}). The Čerenkov radiation is reflected by mirrors within the HGC drum onto PMT detectors which help distinguish if the charged particle is an electron or pion by comparing Čerenkov radiation momentum thresholds.

The aerogel Čerenkov detectors are used to separate pion from protons at high momentum ($p_p > 3$ GeV/c) and work on principles similar to the HGC detectors. They are filled with silicon aerogel material, whose index of refraction can be chosen to be from $n = 1.015$ to 1.05.

The lead glass calorimeter is used to provide additional particle identification/separation. When electrons enter the lead glass calorimeter, they release more bremsstrahlung radiation than pions because of their much smaller mass. Also, pions deposit a constant a amount of energy via ionization in contrast to the electron's sporadic energy deposition in the calorimeter. For electrons, the bremsstrahlung process dominates over the ionization energy loss.

1.3 SIMC

The standard Hall C Monte Carlo package (SIMC) is the software used to simulate the physics processes $p(e, e'p)X$ in this work. Input files provide SIMC with the necessary physics parameters, such as particle mass, kinematics settings, target parameters, spectrometer acceptances, and spectrometer offsets, to run simulations.

For each event, the coordinates of the interaction vertex (x, y, z) and the initial energy (E) and three-momentum ($\vec{p}$) are generated. SIMC's random generation limits for initial angles and momenta are specified by the input file to exceed spectrometer acceptance. This allows events up the acceptance limits to be simulated. It is important to mention that the spectrometers have their own coordinate system. The coordinates used are explained in Figure 11.

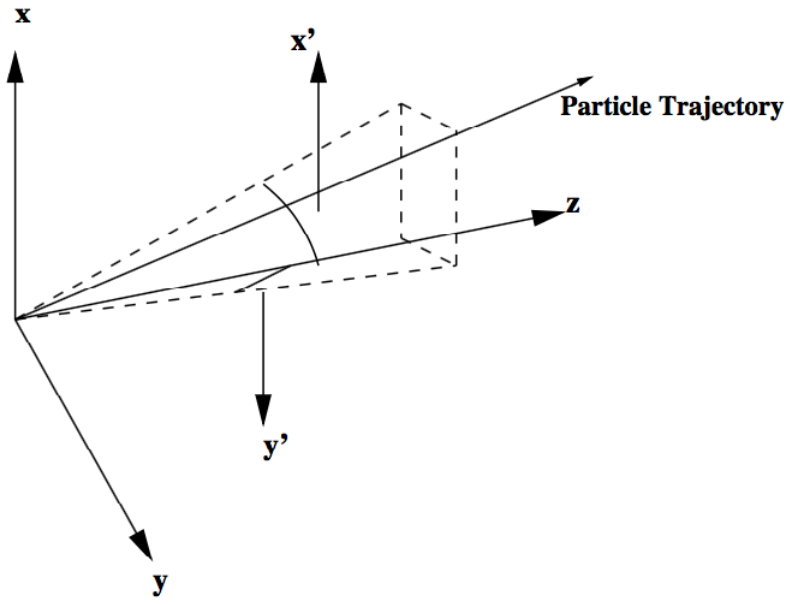

Figure 11: A diagram of the spectrometer coordinate system. $\hat{z}$ always points in the direction of the optical axis, $\hat{x}$ points in the direction of increasing momentum, which for these dipole fields is downwards, and $\hat{y}$ points in the direction given by the right-hand-rule, $\hat{y} = \hat{z} \times \hat{x}$, i.e. to the left of the spectrometers. [7]

The tracking of the outgoing particles are simulated with HMS and SHMS subroutines. Both subroutines take into account energy loss and multiple scattering processes on their way out of the target chamber, past the three quadrupole magnets and single dipole magnet, into the detector hut.

Only events within all spectrometer apertures and events which cross the minimum number of detectors in the huts (that includes all four planes of hodoscopes, and for electrons, the lead calorimeter as well) are considered valid triggers. An event's simulation will cease if a valid trigger is not generated. When a valid trigger is generated, backward reconstructions of the target quantities, x'_{tar}, y'_{tar}, x_{tar}, y_{tar}, and δ are performed. x'_{tar} and y'_{tar} (radians) are the same variables as those defined in Figure 11, but with their reference frame being the target. x_{tar} and y_{tar} (radians) correspond to the point of origin at the target. δ (%) expresses the particles momentum in terms of a fractional difference compared to the central momentum setting of the spectrometer,

$$\delta = \frac{p_{p',e'} - p_0}{p_0}. \tag{1.12}$$

The backward reconstructions of theses target quantities weights the event by a cross section model corrected for radiative processes and by a luminosity factor. These quantities can be compared to experimental data to test cross section model accuracy.

Chapter 2

Methodology

This work consists of using SIMC as a tool to estimate the $\pi^0, \eta, \rho, \omega, \eta', \phi$ yields within the acceptance of the HMS and SHMS for experiment E12-09-011 at Jefferson Lab Hall C [2]. Simulations for these six mesons, as well as a two pion random phase space term, *xphsp*, were simulated with 500,000 successful events for each of the kinematic settings listed in Table 1.2. CERN's data analysis framework, ROOT, was used to manipulate the SIMC generated data.

2.1 Spectrometer Acceptance Cuts

Spectrometer acceptance is a function of reconstruction quantities, $x'_{tar},\ y'_{tar},\ y_{tar},$ and δ. Events with reconstruction quantities outside spectrometer specific limits (see Table 2.1) have to be removed from the SIMC generated data because they are at the edges of the HMS and SHMS observable limits and have low reconstruction efficiency. The removal of SIMC generated data beyond these limits is known as spectrometer acceptance cuts. The values

for HMS cuts come from experimental data taken in the past, while the SHMS cuts rely on design specifications due to the SHMS being a brand new spectrometer.

Spectrometer Acceptance Cuts	
Variable	Value
HMS $\|\delta\|$	$\|$hsdelta$\| < 8.0$ %
HMS $\|x'_{tar}\|$	$\|$hsxptar$\| < 0.080$ rad
HMS $\|y'_{tar}\|$	$\|$hsyptar$\| < 0.035$ rad
SHMS $\|\delta\|$	$\|$ssdelta$\| < 15.0$ %
SHMS $\|x'_{tar}\|$	$\|$ssyptar$\| < 0.024$ rad
SHMS $\|y'_{tar}\|$	$\|$ssxptar$\| < 0.040$ rad

Table 2.1: Spectrometer acceptance cuts applied to all SIMC generated data. [8]

2.2 Diamond Plots

In addition to the spectrometer cuts in Table 2.1, weight and normalization factors are also applied to the SIMC generated data for each setting. Although SIMC stops simulating events which do not make it to the detector hut, it maintains these unsuccessful events, along with successful events, to create a distribution of weight factors. This weight factor distribution alters the data distribution based on the likelihood of a particular event occurring. The normalization factor normalizes data to have a total electron beam charge of 1 mC, i.e. it predicts the actual number of observed coincidence events (for an input cross section after 1 mC of electron beam has passed through Hall C).

In Section 1.2, it was mentioned that kinematic settings are chosen in pairs that have the same W, Q^2, $-t$, and x_B, but different ϵ, to allow for the extraction of separated cross sections using Rosenbluth separation. The $W - Q^2$ (diamond) plot in Figure 10 shows the effects of changing the virtual photon polarization factor, ϵ. The black distribution is for

the high ϵ setting, and the red distribution is for the low ϵ setting. Figure 10 is what results from having spectrometer acceptance cuts, weight factors, and normalization factors applied to both distributions, as well as an extra cut on the low ϵ diamond perimeter to remove its event-scarce borders. It illustrates the amount of experimental data that will be useful for the calculations of $p(e,e'p)X$ cross sections, and the large amount of data that will be discarded because it cannot be used to determine LT-separated cross sections.

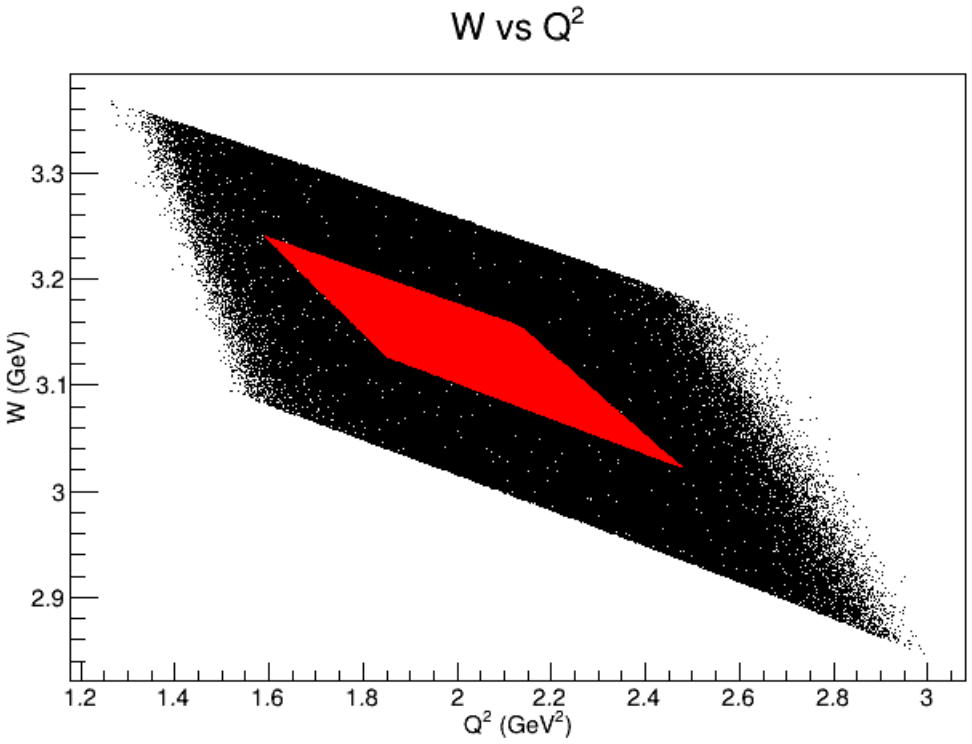

Figure 10: The simulation diamond plot for the $p(e,e'p)\omega$ reaction. $Q^2 = 2.00$ GeV^2, $W = 3.14$ GeV^2, $\epsilon_{\text{red}} = 0.395$, $\epsilon_{\text{black}} = 0.752$, $\theta_q = 6.20$ deg.

2.3 Missing Mass

To calculate the anticipated production yields of backward angle mesons, $\pi^0, \eta, \rho, \omega, \eta', \phi$, missing mass plots are constructed with spectrometer acceptance cuts, weight factors, nor-

malization factors, as well as the fore-mentioned low ϵ diamond perimeter cut, applied to them. This gives the number of events which allow the extraction of separated cross sections.

Production yields are retrieved from missing mass plots for each meson, X, at each kinematic setting. This is done by integrating over the missing mass's full width at half maximum. The production rates are calculated by $r = \text{yield}/t$, where t is the time required for the electron beam, with current $I = 70\ \mu A$, to produce a total charge of $Q_{tot} = 1$ mC ($t = Q_{tot}/I = 1$ mC$/70\ \mu A = 14.28$ s).

A linear-scale plot is shown for the setting $Q^2 = 2.00$ GeV^2, $W = 3.14$ GeV, $\epsilon = 0.395$, θ_q = 6.20 deg in Figure 11. The vertical lines represent where a meson's accepted mass value

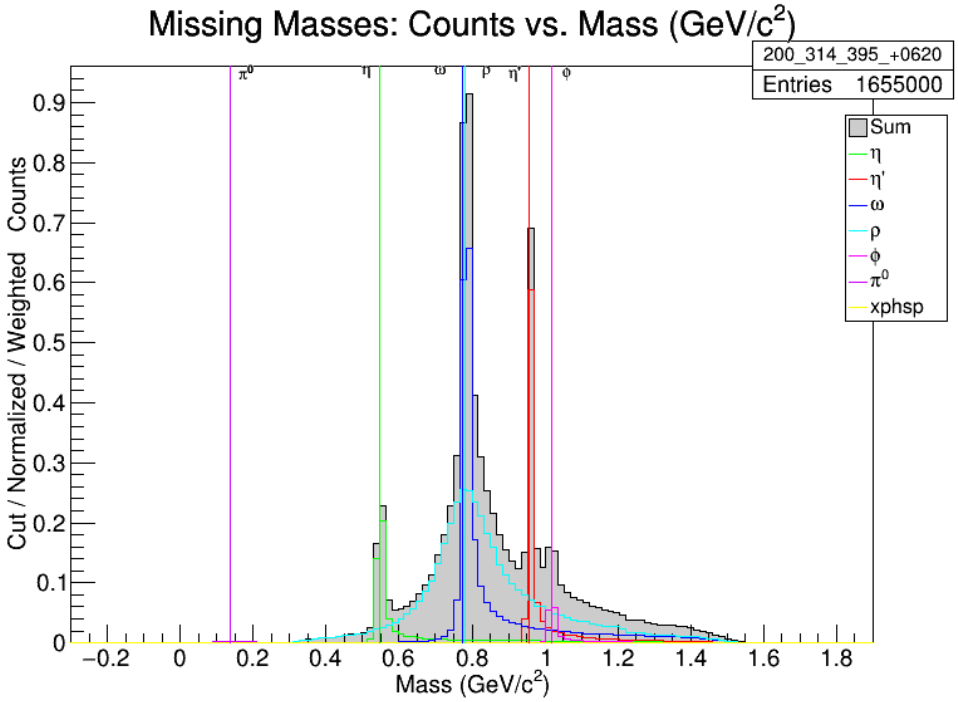

Figure 11: A reconstructed missing mass linear-scale plot for $Q^2 = 2.00$ GeV^2, $W = 3.14$ GeV, $\epsilon = 0.395$, $\theta_q = 6.20$ deg. This is to give an idea of what a linear-scale plot would look like since all other missing mass plots are on a log-scale.

is located. It is difficult to recognize features on linear-scale plots because ω and ρ yields are, for the majority of settings, much larger than other meson yields. With log-scale plots,

missing mass features are more apparent.

Included in this paper are log-scale missing mass plots for high and low ϵ at three different settings:

Q^2 (GeV^2)	W (GeV)	Figures $\epsilon_{Low},\ \epsilon_{High}$
0.40	2.45	13, 14
2.00	3.14	15, 16
5.50	3.02	17, 18

Table 2.2: The Q^2 and W settings for the log-scale missing mass plots in this paper. For each setting there is a high and low ϵ setting included.

These plots are included to show how the missing mass distributions evolve with increasing Q^2 and W.

After cuts have been applied to high and low ϵ diamonds, the low ϵ diamonds have more entries than their high ϵ diamond counterparts. The same number of events are simulated for high and low ϵ, but the high ϵ diamond coverage is much larger than the low ϵ diamond coverage, resulting in a lower event density in the overlapping low ϵ region (the only region where we can extract longitudinal and transverse cross sections). The number of events here only indicates the statistical precision of the Monte Carlo simulation. Additionally, the normalized y-axis values give the expected event yields, which are actually larger at high ϵ than low ϵ.

Besides fewer high ϵ entries, the diamond cuts also introduced more sporadic missing masses distributions for high ϵ. For example, the ω distribution at 0.2 GeV in Figures 15 and 16 have spikes. Again, this is due to the statistical precision of the Monte Carlo simulation and is related to the number of simulated events.

The relative normalization of the different peaks comes from the models implemented in SIMC. They are based on extrapolations of previous data and may not be very accurate for these kinematics.

There are negative missing mass values for π^0 at multiple settings because π^0's missing masses are small and the simulated experimental resolution produces smearing across 0 GeV. The dip at 0 GeV is an artifact of the square-root function when going from $(M_m)^2$ to M_m.

The overall width of the missing mass distributions is decreased from applying spectrometer acceptance cuts. Figure 12, in contrast to Figure 13, demonstrates this.

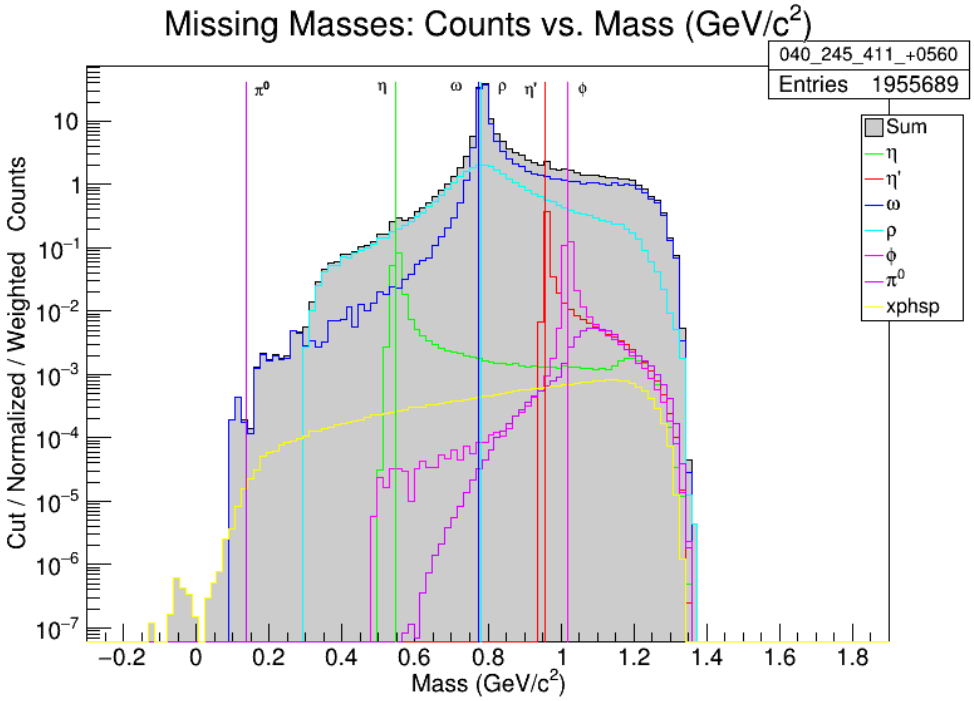

Figure 12: A reconstructed log-scale missing mass plot for $Q^2 = 0.40$ GeV^2, $W = 2.45$ GeV, $\epsilon = 0.411$, $\theta_q = 5.60$ deg without spectrometer cuts. This demonstrates how the width of the distribution is effected by spectrometer acceptance cuts. This distribution is much wider than the same distribution with spectrometer acceptance cuts in Figure 13.

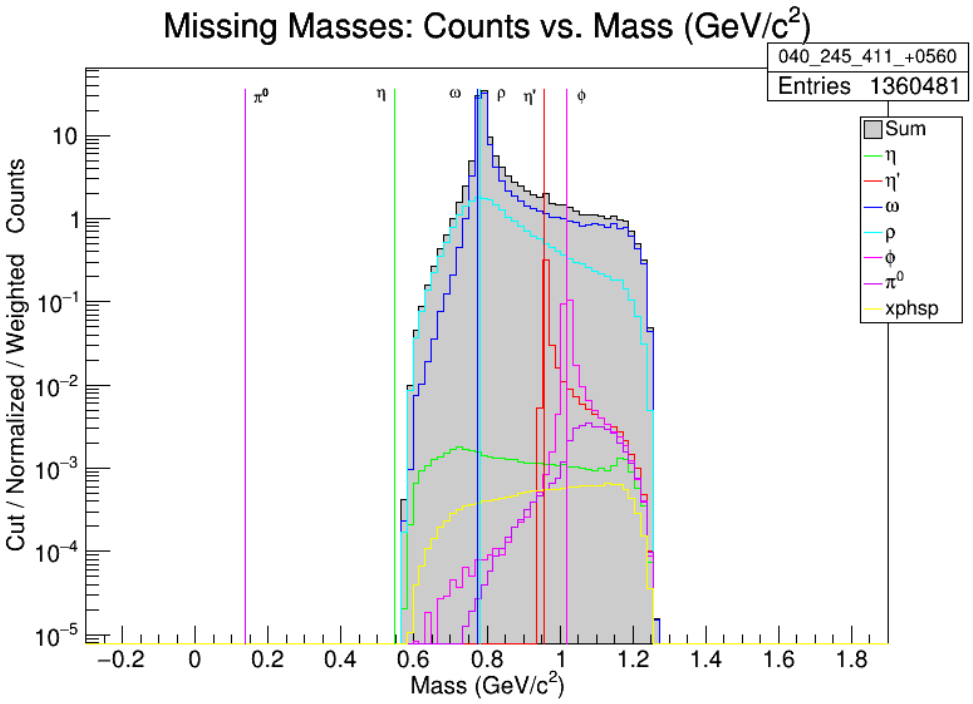

Figure 13: A reconstructed log-scale missing mass plot for $Q^2 = 0.40$ GeV^2, $W = 2.45$ GeV, $\epsilon = 0.411$, $\theta_q = 5.60$ deg.

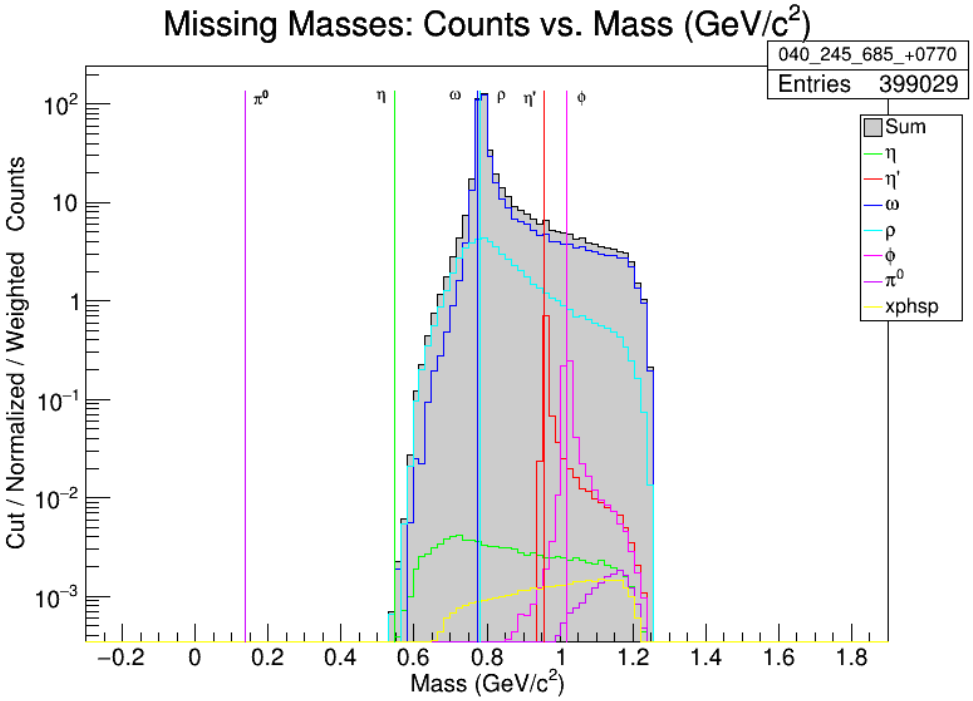

Figure 14: A reconstructed log-scale missing mass plot for $Q^2 = 0.40$ GeV^2, $W = 2.45$ GeV, $\epsilon = 0.685$, $\theta_q = 7.70$ deg.

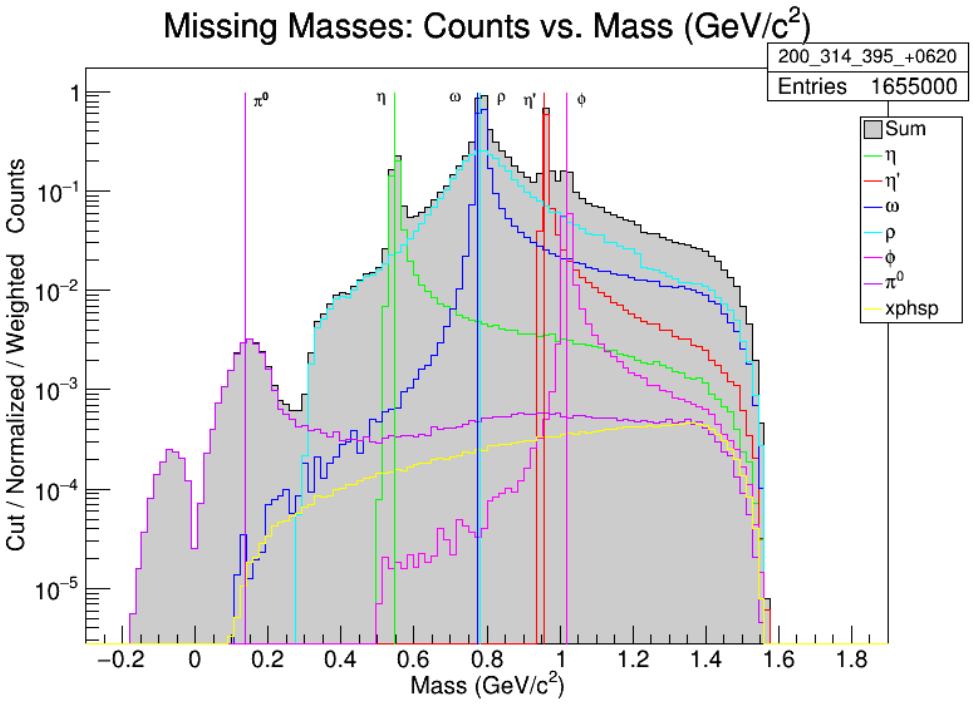

Figure 15: A reconstructed log-scale missing mass plot for $Q^2 = 2.00$ GeV^2, $W = 3.14$ GeV, $\epsilon = 0.395$, $\theta_q = 6.20$ deg.

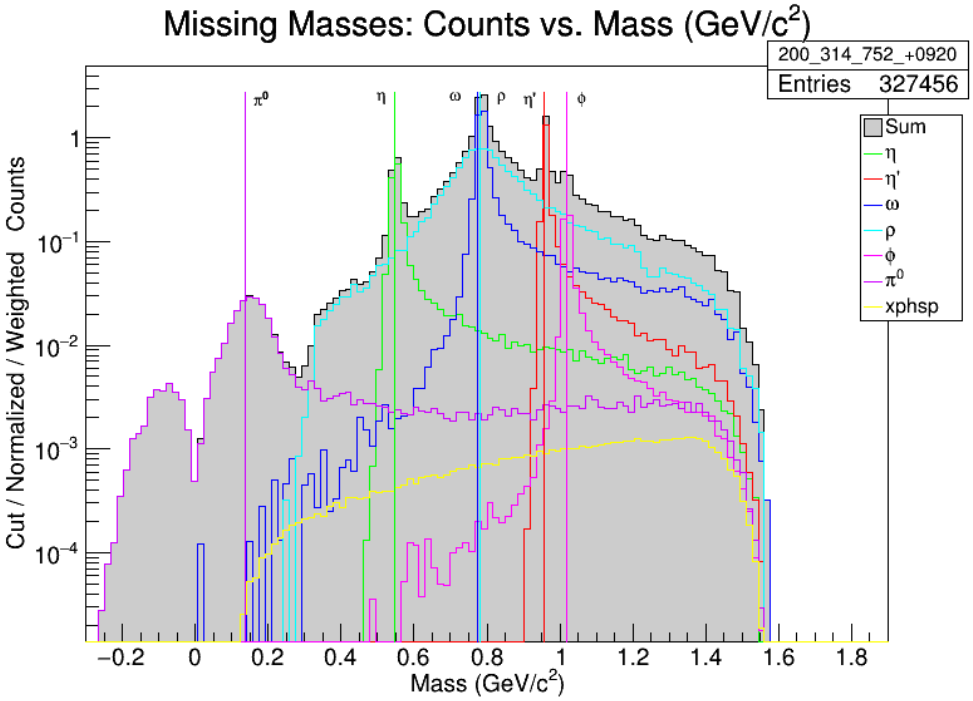

Figure 16: A reconstructed log-scale missing mass plot for for $Q^2 = 2.00$ GeV^2, $W = 3.14$ GeV, $\epsilon = 0.752$, $\theta_q = 9.20$ deg.

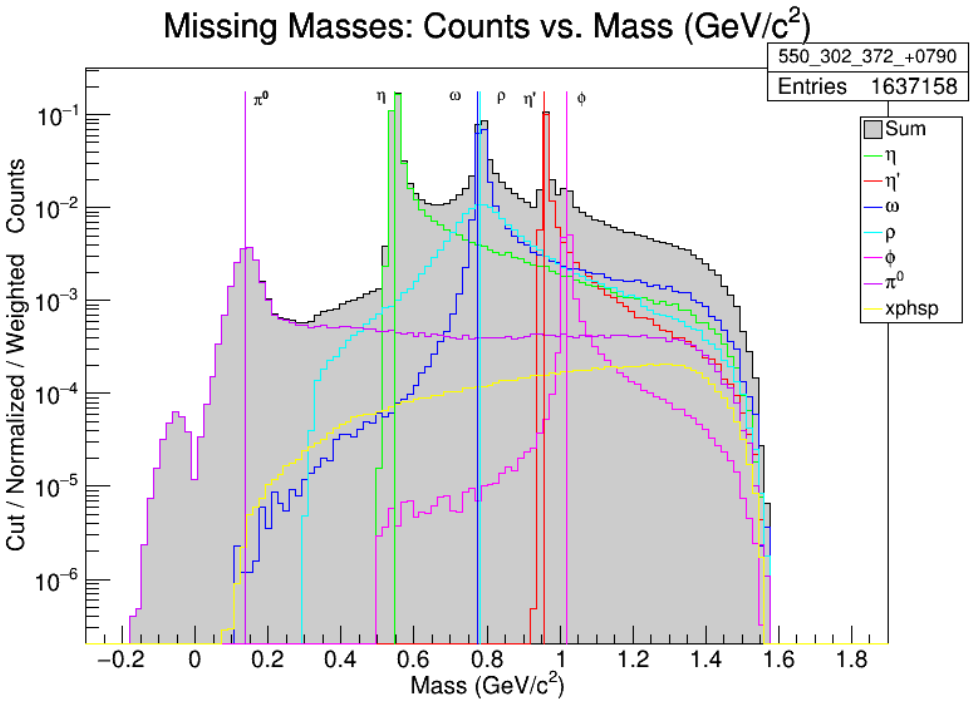

Figure 17: A reconstructed log-scale missing mass plot for $Q^2 = 5.50$ GeV^2, $W = 3.02$ GeV, $\epsilon = 0.372$, $\theta_q = 7.90$ deg.

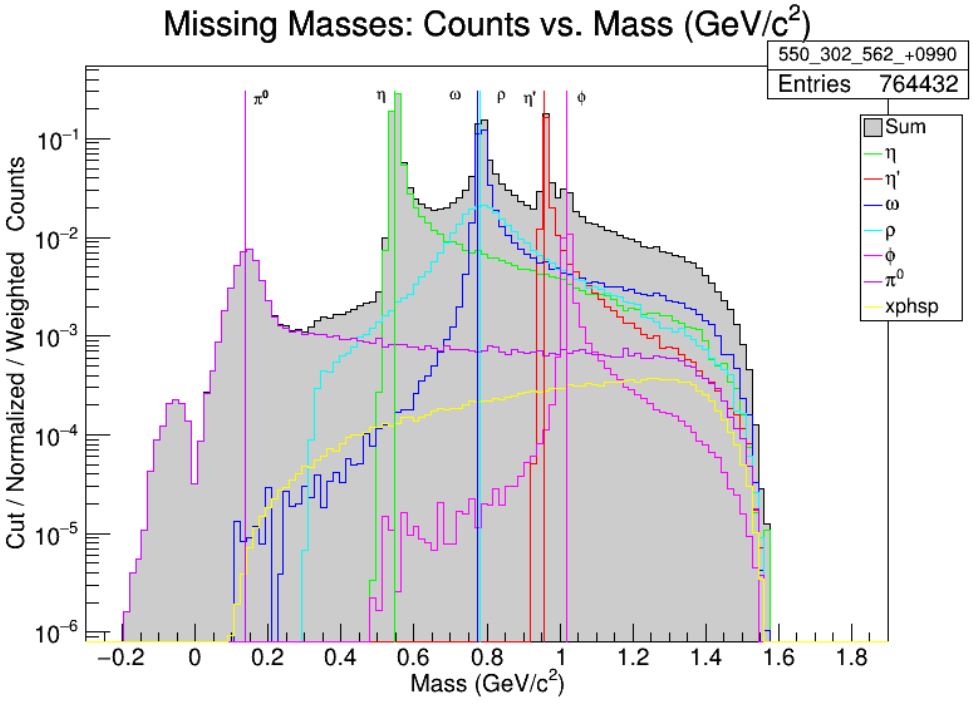

Figure 18: A reconstructed log-scale missing mass plot for $Q^2 = 5.50$ GeV^2, $W = 3.02$ GeV, $\epsilon = 0.562$, $\theta_q = 9.90$ deg.

Table 2.3 outlines which settings have adequate coverage of missing mass distributions. This is based on whether the mesons, X, have their peaks aligned with their accepted mass values, and whether each meson has healthy yield characteristics. For example, in the missing mass log-plot of $Q^2 = 4.40$ GeV^2, $W = 2.74$, and $\epsilon = 0.479$, shown in Figure 19, π^0 is below its "background" distribution, and is not considered to have adequate coverage.

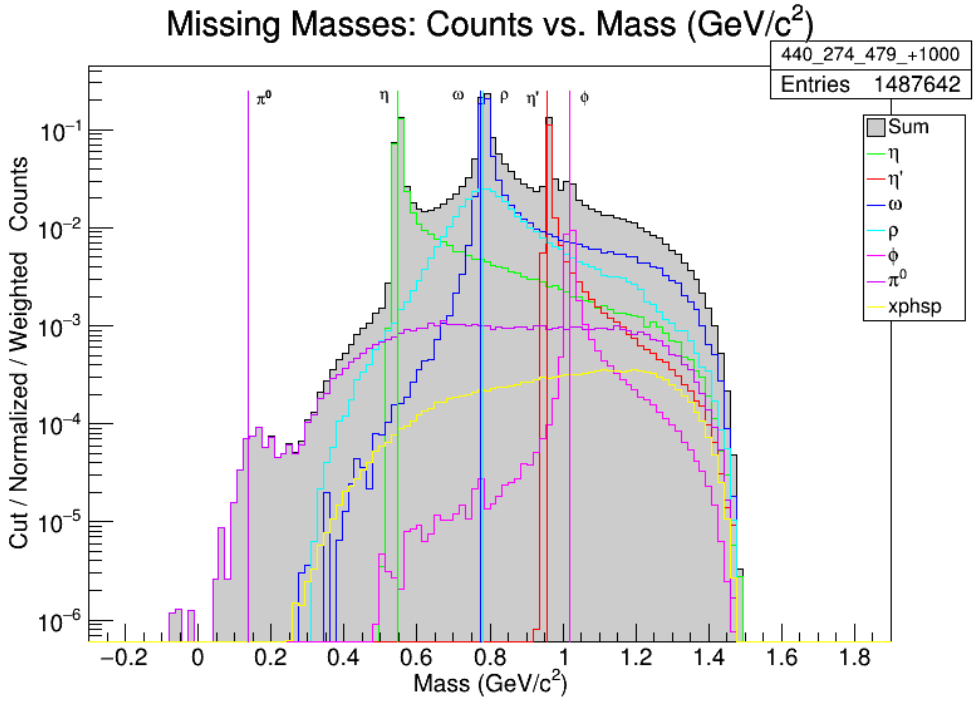

Figure 19: A reconstructed log-scale missing mass plot for $Q^2 = 4.40$ GeV^2, $W = 2.74$, and $\epsilon = 0.479$, $\theta_q = 10.00$ deg.

Q^2 (GeV^2)	W (GeV)	ϵ
1.25	3.14	0.492
1.25	3.14	0.699
2.00	3.14	0.395
2.00	3.14	0.580
2.00	3.14	0.752
3.00	3.14	0.391
3.00	3.14	0.691
3.50	3.37	0.364
3.50	3.37	0.557
4.40	2.74	0.735
5.50	3.02	0.372
5.50	3.02	0.562

Table 2.3: A table of settings with adequate missing mass coverage for mesons, X. The main limiting factor was the π^0 meson not having yields above 10^{-3} events/mC.

If we disregard π^0, adequate missing mass coverage is achieved for each meson above Q^2 = 0.40 GeV^2. If we disregard π^0, and η at Q^2 = 0.40 GeV^2, we have adequate missing mass coverage for each meson at each setting. η's poor coverage at Q^2 = 0.40 GeV^2 is shown in Figures 13 and 14.

To summarize, these missing mass plots provide us with information that tells us which kinematic settings, and for which backward-angle mesons, complementary data from experiment E12-09-011 is feasible.

Chapter 3

Results and Discussion

3.0.1 $W - Q^2$ Coverage

In this work, each kinematic setting's diamond plot had overlapping low and high ϵ distributions with the exception of the ϕ-meson with $Q^2 = 3.00$ GeV^2, $W = 2.32$ GeV, ϵ, $= 0.634$, $\theta_q = 14.1$ deg shown in Figure 20. It's high ϵ diamond has an unnatural event density transition as it extends towards $W = 2.00$ GeV. This indicates that the W dependence in the ϕ-production physics model in SIMC, for this particular setting, requires revising.

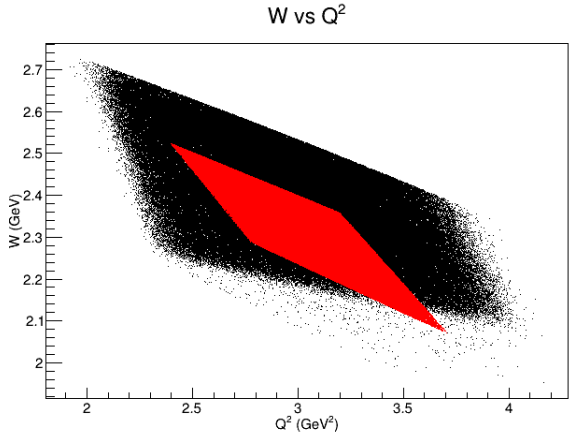

Figure 20: ϕ-meson diamond plot with $Q^2 = 3.00$ GeV^2, $W = 2.32$ GeV, $\epsilon_{\text{red}} = 0.634$, $\epsilon_{\text{black}} = 0.888$, $\theta_q = 14.1$ deg.

Figure 21 shows the density of η's high ϵ diamond changing halfway between invariant mass, W, indicating potential W dependence issues in the η-production physics model.

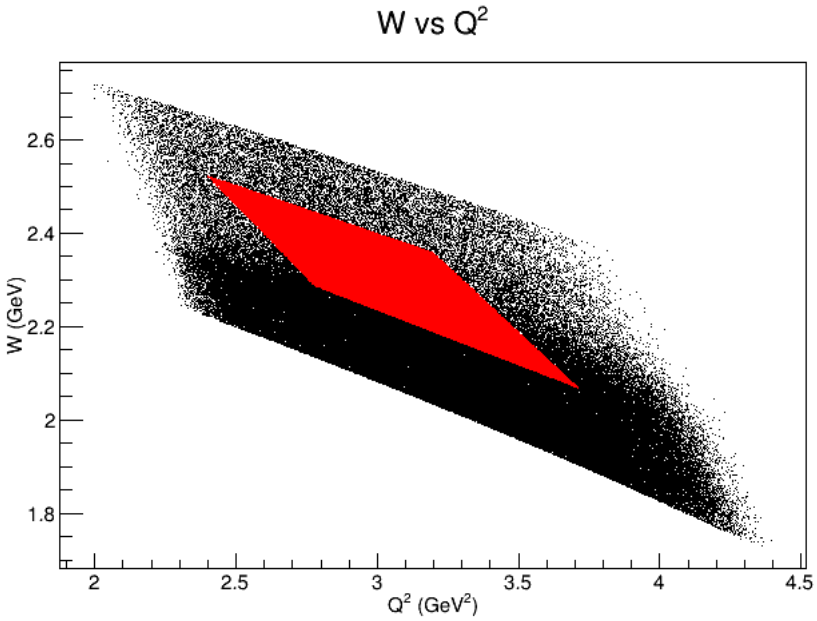

Figure 21: η-meson diamond plot with $Q^2 = 3.00$ GeV^2, $W = 2.32$ GeV, $\epsilon_{\text{red}} = 0.634$, $\epsilon_{\text{black}} = 0.888$, $\theta_q = 14.1$ deg.

Other than these shortcomings, these plots illustrate that the extraction of separated cross sections is promising for all settings.

3.0.2 Missing Mass

The missing mass plots demonstrate that it should be possible to reconstruct the missing mass of mesons produced in $p(e, e'p)\pi^0, \eta, \rho, \omega, \eta', \phi$ reactions for most settings. This is because at most kinematic settings, SIMC's missing mass distributions have peaks coinciding with accepted meson masses, and the missing mass coverage is adequate. Table 2.3 listed the settings with adequate missing mass coverage for each meson. π^0 had the limiting missing mass distribution coverage for all cases.

3.0.3 Rates

By comparing the updated beam time estimates for 10,000 good events in experiment E12-09-001 from [7] (Table A.1) with the time estimates from this work, the feasibility of studying particular backward angle mesons, based on kinematic settings, can be determined. From this method, it was concluded that ω and ρ are almost entirely within the time limits for 10,000 events to occur, with the exception of 2 and 3 settings respectively; η and η' are feasible to study at some kinematic settings with $Q^2 \geq 3.00$ GeV^2, and ϕ and π^0 are not feasible to study. Table 3.1 consists of the updated beam time schedule for each setting and the predicted beam times for each setting to produce 10,000 successful events. Table 3.2 lists the settings which are only within the scheduled beam time.

It is expected ω will have the best statistics because of its narrow missing mass signature near the center of the spectrometer momentum range, and its high production rate.

Setting Number	Q^2 (GeV^2)	W (GeV)	ϵ	Allocated Time (Hrs.)	Time (Hrs.) η	η'	ω	ρ	ϕ	π^0
1	0.40	2.45	0.411	10.3	1898.4	122.6	0.7	2.9	201.66	inf
2	0.40	2.45	0.685	13.6	943.9	54.7	0.2	1.2	85.34	inf
3	1.25	3.14	0.492	9.4	44.8	21.6	7.8	2.5	64.06	1199.98
4	1.25	3.14	0.699	8.0	23.1	12.1	3.7	1.3	32.24	378.68
5	1.70	2.45	0.595	19.6	1219.5	124.9	10.6	20.3	486.16	inf
6	1.70	2.45	0.856	12.2	263.0	64.6	4.6	8.1	213.74	45225.70
7	2.00	3.14	0.395	38.3	115.1	63.2	31.4	18.6	344.49	3060.01
8	2.00	3.14	0.752	21.6	41.0	26.7	11.5	5.9	114.01	250.86
9	3.00	2.32	0.634	50.0	3416.9	414.9	24.7	76.2	1381.28	inf
10	3.00	2.32	0.888	32.0	496.7	199.2	8.1	24.8	524.57	6807.34
11	3.00	3.14	0.391	73.6	127.4	95.4	83.2	59.4	816.85	1515.39
12	3.00	3.14	0.691	49.4	52.1	43.7	34.0	20.9	292.43	475.85
13	3.50	3.37	0.364	100.8	101.0	81.4	131.9	75.8	889	1598.83
14	3.50	3.37	0.557	90.2	58.0	48.9	74.5	38.2	445.49	718.10
15	4.40	2.74	0.479	115.8	196.9	335.9	101.6	188.8	2196.72	5547.05
16	4.40	2.74	0.735	93.6	83.0	172.9	45.6	75.5	883.88	558.03
17	5.50	3.02	0.372	297.1	144.2	378.9	296.6	441.6	3981.87	3126.93
18	5.50	3.02	0.562	295.3	83.9	227.2	167.4	223.6	1920.19	1552.63

Table 3.1: The time required to produce 10,000 successful events with the specified kinematic settings assuming 70 μA beam current on a 10 cm LH_2 target. The "Allocated Time (Hrs.)" is the updated beam time estimates for E12-09-011 and they are taken from [7].

Figures 22 and 23 illustrate the times from Table 3.1. From these figures, it is evident that higher ϵ settings are more efficient than lower ϵ because they require less allocated beam time. It is also evident that with higher Q^2, the amount of allocated beam time required increases, although this is not precisely true for π^0 and η.

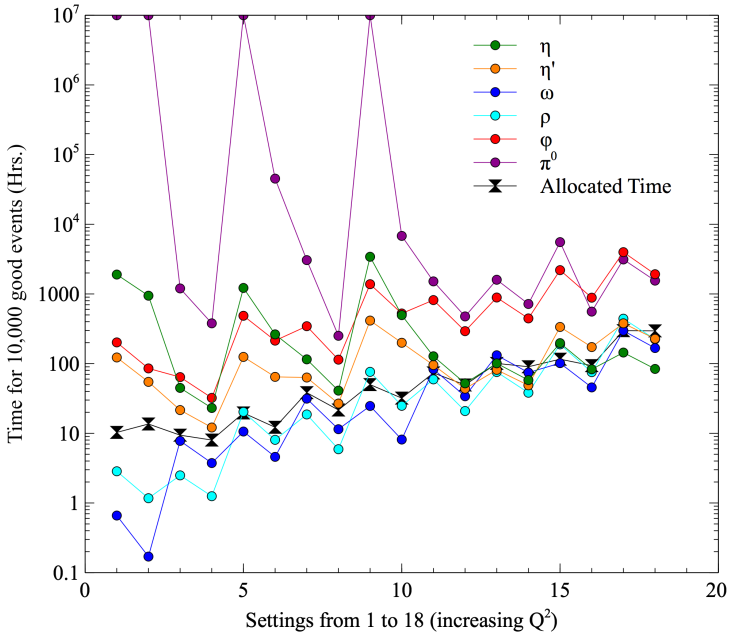

Figure 22: The time required for 10,000 good events based on the missing mass plots (normalized and with cuts) generated by SIMC. All mesons, X, are included in this plot, as well as the updated beam times for each setting from [7] (Table A.1). Note the y-axis is on a log-scale.

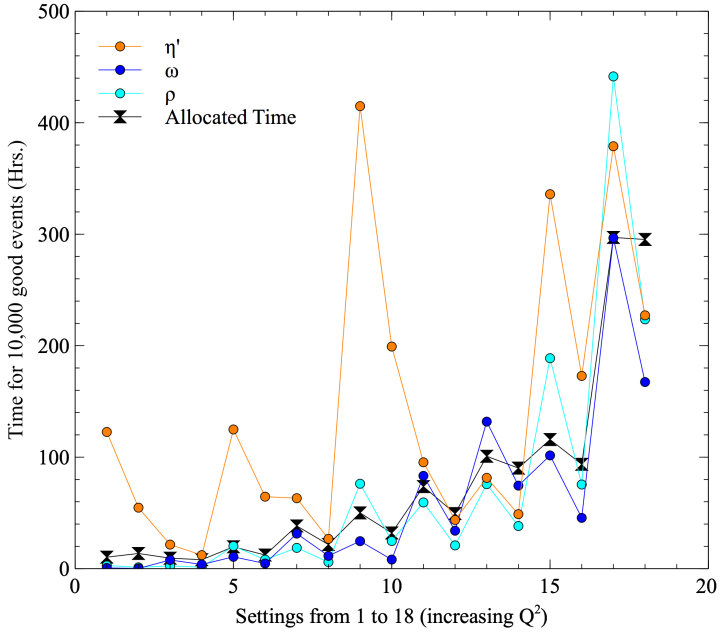

Figure 23: The time required for 10,000 good events based on the missing mass plots (normalized and with cuts) generated by SIMC. η', ω, and ρ are the only mesons included in this plot because they are the settings with times consistently close to the updated beam times. Updated beam times for each setting from [7] (Table A.1).

Finally, if the settings are within the allocated beam time, they are listed in Table 3.2. This table is ultimately the objective of this work. Its values are the same as in Table 3.1, except if the predicted times are large than the estimated times, they are not displayed. This table clearly shows which mesons should be able to give statistically significant complementary data in experiment E12-09-011.

Combining the illustrative power of the missing mass plots and Table 3.2 gives us a strong indication that obtaining complementary data for ω and ρ is feasible at the majority of settings, while η and η' are feasible to study at 4 settings each, and ϕ and π^0 are not feasible to study.

Setting Number	Q^2 (GeV^2)	W (GeV)	ϵ	Allocated Time (Hrs.)	Time (Hrs.) η	η'	ω	ρ	ϕ	π^0
1	0.40	2.45	0.411	10.3			0.7	2.9		
2	0.40	2.45	0.685	13.6			0.2	1.2		
3	1.25	3.14	0.492	9.4			7.8	2.5		
4	1.25	3.14	0.699	8.0			3.7	1.3		
5	1.70	2.45	0.595	19.6			10.6			
6	1.70	2.45	0.856	12.2			4.6	8.1		
7	2.00	3.14	0.395	38.3			31.4	18.6		
8	2.00	3.14	0.752	21.6			11.4	5.9		
9	3.00	2.32	0.634	50.0			24.7			
10	3.00	2.32	0.888	32.0			8.1	24.8		
11	3.00	3.14	0.391	73.6				59.4		
12	3.00	3.14	0.691	49.4		43.7	34.0	20.9		
13	3.50	3.37	0.364	100.8		81.4		75.8		
14	3.50	3.37	0.557	90.2	58.0	48.8	74.4	38.2		
15	4.40	2.74	0.479	115.8			101.6			
16	4.40	2.74	0.735	93.6	83.0		45.5	75.5		
17	5.50	3.02	0.372	297.1	144.2		296.6			
18	5.50	3.02	0.562	295.3	83.9	227.2	167.4	223.6		

Table 3.2: The time required to produce 10,000 successful events with the specified kinematic settings assuming 70 μA beam current on a 10 cm LH_2 target. The "Allocated Time (Hrs.)", or LH_2 time (Hrs.), is the updated beam time estimates for E12-09-011 and they are taken from [7]. Times are not displayed if they are larger than the allocated times.

An explanation as to why ω and ρ rates are higher than the other mesons is that their masses are in the center of the missing mass plots ($M_m \approx 0.78$ GeV/c^2). This is significant, because the spectrometer momentum range has the most acceptance near its center. Events on the edges of this range, which corresponds to missing mass distributions, are cut off (demonstrated in Figures 12 and 13 at $Q^2 = 0.40$ GeV/c^2). This means the mass/energy regions of ω and ρ are optimal for studying at Hall C.

3.0.4 Future Work

Currently, Q^2 and W are being extrapolated into regions where these physics processes have not yet been observed. The models used will need revising to create $W-Q^2$ distributions which are qualitatively and quantitatively more likely.

Since the feasibility of studying backward-angle mesons has been shown for experiment E12-09-011, other upcoming Hall C experiments could also have complementary data studies done, perhaps for other kinematic settings, or other mesons besides those considered in this work.

Bibliography

[1] Henley, Ernest M., et al. Subatomic Physics 3rd Ed. World Scientific, 2008.

[2] Jefferson Lab E12-09-011 "Studies of the L-T Separated Kaon Electroproduction Cross Section from 5-11 GeV", T. Horn, G.M. Huber, P. Markowitz (spokespersons), https://www.jlab.org/exp_prog/proposals/09/PR12-09-011.pdf

[3] Siegfried Bethke, Experimental Tests of Asymptotic Freedom, arXiv:hep-ex/0606035.

[4] Wenliang Li, *Exclusive Backward-Angle Omega Meson Electroproduction*, Ph.D. Thesis, University of Regina, 2017.

[5] K.A. Lovie et al, "Review of Particle Physics," *Particle Data Group, Chin. Phys.,* vol C38, 2014.

[6] Meziani, Z.E. et al. arXiv:1609.00676 [hep-ex] PR12-16-007, JLAB-PHY-16-2358

[7] Samip Basnet, *Deep Exculsive Pseudoscalar Meson Production at Jefferson Lab Hall C* M.Sc. Thesis, University of Regina, 2017.

[8] *pre-Conceptual Design Report*, (*pCDR*), SURA, 2004. Jefferson Lab Upgrade.

[9] D.G. Meekins, *Coherent π^0 photoproduction on deuteron.* Ph.D. Thesis, College of William and Mary, 1998.